J. Fluid Mech. (1986), *vol.* 171, *pp.* 459–476
Printed in Great Britain

Rip-current generation near structures

By H. G. WIND AND C. B. VREUGDENHIL
Delft Hydraulics Laboratory, Laboratory de Voorst, P.O. Box 152, 8300 AD Emmeloord, The Netherlands

(Received 9 February 1985 and in revised form 28 September 1985)

Data have been obtained for a wave-driven current system in a closed basin. Owing to interaction of the longshore current with the sidewall a strong rip current was generated. The velocity distribution over the depth of the rip current appeared to be more or less uniform. The current system has been modelled by means of a mathematical model. The effect of bottom topography, bottom friction, convection and turbulent viscosity on the current system has been investigated. The conclusions are that the rip current is dominated by convection and that the bottom topography plays a role in the convergence and divergence of the streamlines. The order of magnitude of the velocities is largely determined by the bottom-friction coefficient. The velocity field is modified by viscosity. First, turbulent viscosity entrains fluid in the longshore current and into the rip current, secondly it permits turbulent boundary layers and thirdly it is responsible for the existence of closed streamlines outside the breaker zone. Finally the model and the conclusions are extrapolated to prototype conditions.

1. Introduction

Along many beaches signs are placed to warn swimmers not to bathe close to the groynes because, under certain conditions, strong rip currents can build up, carrying even strong swimmers offshore up to distances several times the width of the breaker zone.

An example of a rip current near a headland is shown in figure 1, which is a picture of one of the many beaches north of Sydney (Australia). Owing to the oblique incident waves a longshore current is generated. This longshore current runs parallel to the shoreline up to the downstream headland, at which point the longshore current breaks out forming a strong rip current.

Rip currents near harbour moles can have a significant effect on the morphology. In figure 2 the harbour moles of the port of Ravenna are shown. Close to the left mole a sedimentation pattern is visible up to a distance of 1600 m offshore. The question from a hydrodynamic point of view is how to model the flow in order that the rip current extends over such a distance offshore and remains attached to the breakwater. These points are elaborated and verified in this paper.

Streamline patterns of rip currents near a structure are shown in the paper of Dalrymple, Eubanks & Birkmeyer (1977). Visser (1984) presents experimental evidence of a rip current in a closed basin. An attempt to explain the origin of rip currents is made by Bowen (1969). He shows that a longshore variation in wave height can produce a nearshore circulation, consisting of a longshore current feeding a relatively strong rip current and a weak onshore flow. The specific feature of the rip current, namely the high velocities in a narrow zone, is caused by vortex stretching over the sloping bottom topography. An attempt by Bowen (1969) to reproduce the

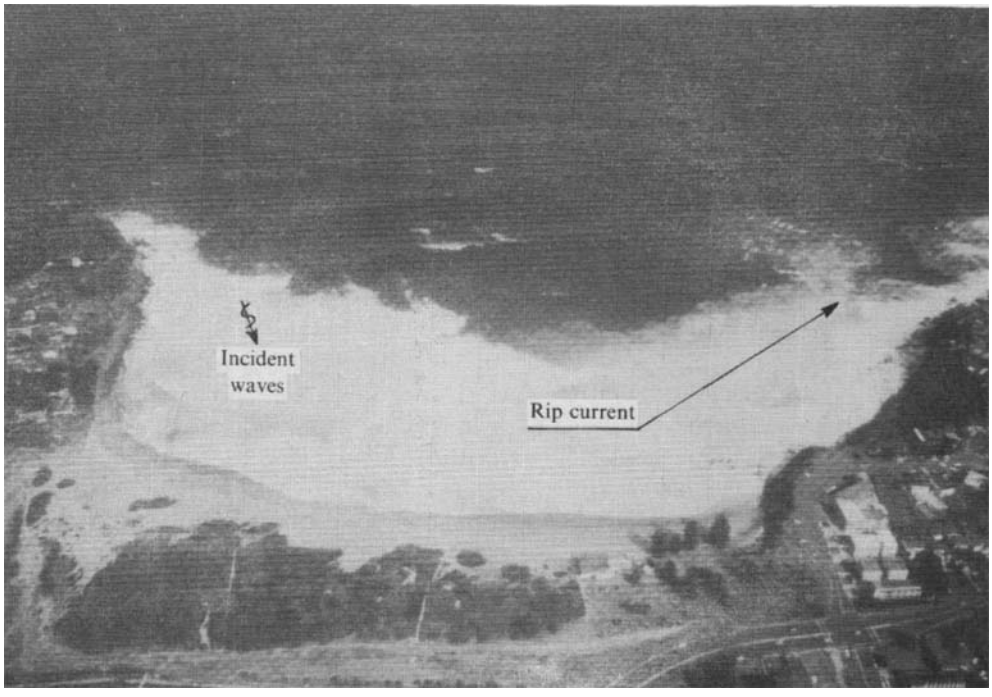

FIGURE 1. Generation of a rip current near a headland in Sydney, Australia (courtesy of Dr P. Cowell).

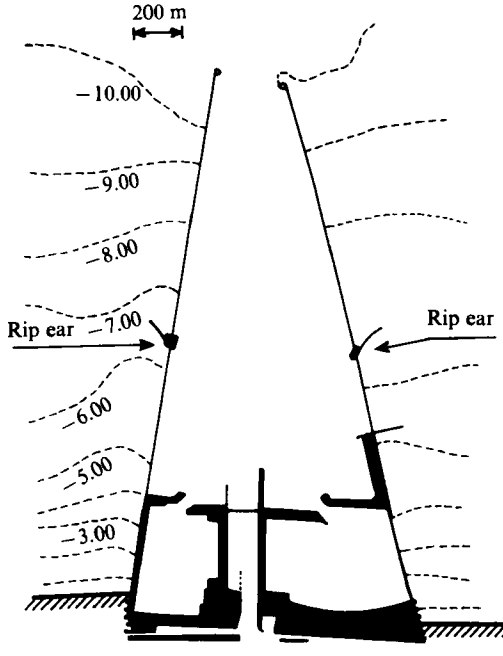

FIGURE 2. Port of Ravenna (Italy) with rip channels and (proposed) rip ears.

high velocities observed in nature in a mathematical model failed because of numerical problems. Subsequently many authors have attempted to model the nearshore-current system including the rip current and although the longshore current can be represented reasonably well, the rip current is either absent or rather weak.

Dalrymple *et al.* (1977) and Liu & Mei (1976) used models in which radiation stresses and bottom friction were present, but convective terms and viscosity were not. These results resemble our figure 11 (*c*) where the same assumptions were made. However, in this paper we show that convective terms are of dominant importance for the behaviour of rip currents and that viscosity is responsible for certain details.

An example of a finite-element model including convective terms and bottom friction was given by Kawahara, Takagi & Inagaki (1980): their computations show two eddies. We show that, in the absence of viscosity, any closed streamline should pass through the breaker zone. It is not clear whether this is true in the results of Kawahara *et al.* (1980). Some numerical viscosity might be present, yielding flow patterns similar to a model including viscous terms, but with an unknown, and possibly unrealistic, viscosity coefficient.

Ebersole & Dalrymple (1979), Wu & Liu (1982), Kawahara & Kashiyama (1984) and Watanabe (1982) have published results for models containing all relevant terms. The second and fourth papers refer to a closed basin similar to ours. However, their numerical results do not show a concentrated rip current. Here, we show that this can be caused by an unrealistically large value of the viscosity coefficient outside the breaker zone (figure 11*d*). It may be that the authors mentioned above did apply such high values. In the first paper a relatively high viscosity coefficient is used, but it is specifically stated that the purpose was to present a stable numerical scheme, and not an attempt to verify the choice of the viscosity coefficients used.

The objectives of the present paper are threefold. The first is to identify the relative importance of convection, diffusion and bottom friction in the process of rip-current formation near a structure. Secondly, an estimate of the order of magnitude of the various coefficients is attempted. The third objective is to generalize the model and conclusions to prototype conditions.

Our study is supported by a simple experiment in a closed wave basin. The advantage of this configuration is that the boundary conditions are well defined. The step from this configuraton to a more complex situation, such as a series of groynes, requires some care. However, as the formulations of bottom friction and diffusion are independent of the geometry, the conclusions are also applicable to a more general geometry such as Ravenna. We made use of a large basin 24×30 m to allow for similar breaking processes in the model as occur on a gentle (1:50) beach in prototype, and furthermore to allow for a free generation of the rip currents over a distance of several times the width of the breaker zone.

The experimental set-up is explained and the velocity distributions measured in the longshore current and rip current are presented in §2. The governing equations and mathematical formulation of the processes are given in §3 and the computed results in §4. In §§5–7, an analysis is given of the importance of these mechanisms, viz. convection, viscosity and bottom friction, supported by various numerical experiments. Some implications for coastal currents occurring in nature are given in §8. The conclusions are summarized in §9.

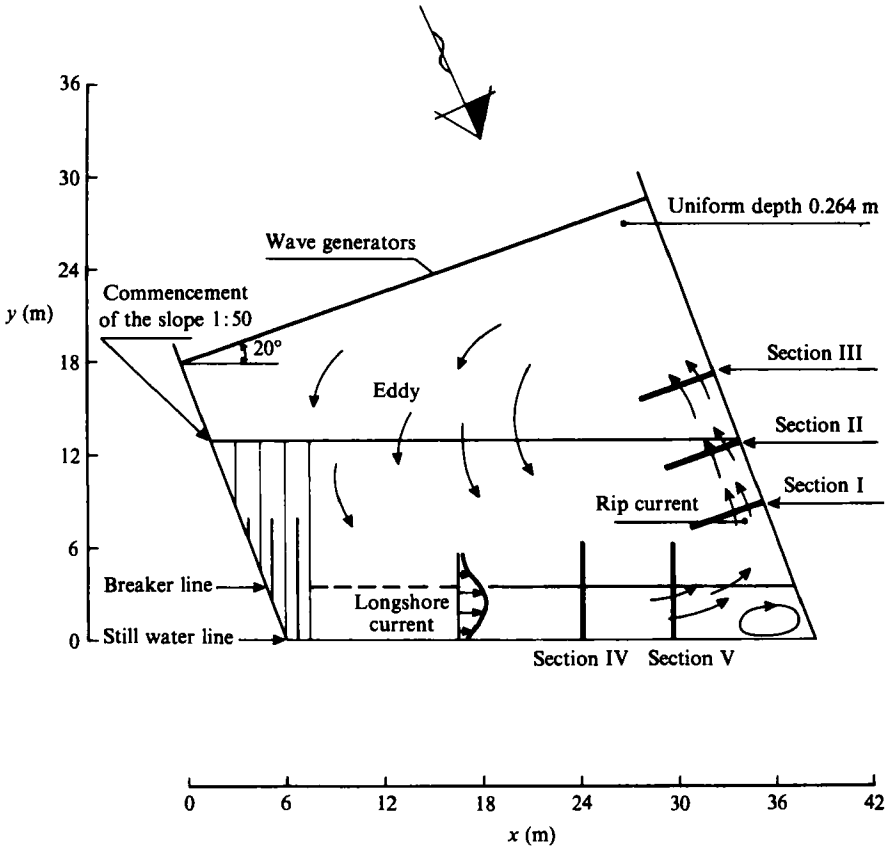

FIGURE 3. Experimental basin consisting of a section with uniform depth and a section with a 1:50 sloping beach.

2. Experimental facility, test conditions and results

2.1. *Experimental facility and test conditions*

The experiments were carried out in the basin shown in figure 3. Wave generators were constructed over the full 30 m width of the constant-depth part of the basin. The average distance between the wave machines and the plane 1:50 slope was 12 m. The angle between the wave generators and the depth contours was 20°. The wave height of the regular waves, H_{rms} and period T in the constant-depth part of the basin were $H_{\mathrm{rms}} = 0.043 \pm 0.002$ m and $T = 1$ s respectively. The mean water depth in front of the wave generators was 0.264 ± 0.007 m.

2.2. *Wavefield and wave set-up*

After propagating over the constant-depth part of the basin, the waves refracted over the plane beach. They reached their maximum height of 0.052 m at a distance of 3.30 m from the still-water line. Spilling breakers then formed which travelled through the surf zone with a breaker index $H/(h+\eta)$, changing from 0.8 at the breaker line to about 0.5 inshore. The wave-height distribution normal to the shore is shown in figure 4(*a*).

A rip current was generated near the sidewall, and in this region the wave field was strongly modified owing to wave–current interaction and wave breaking. The

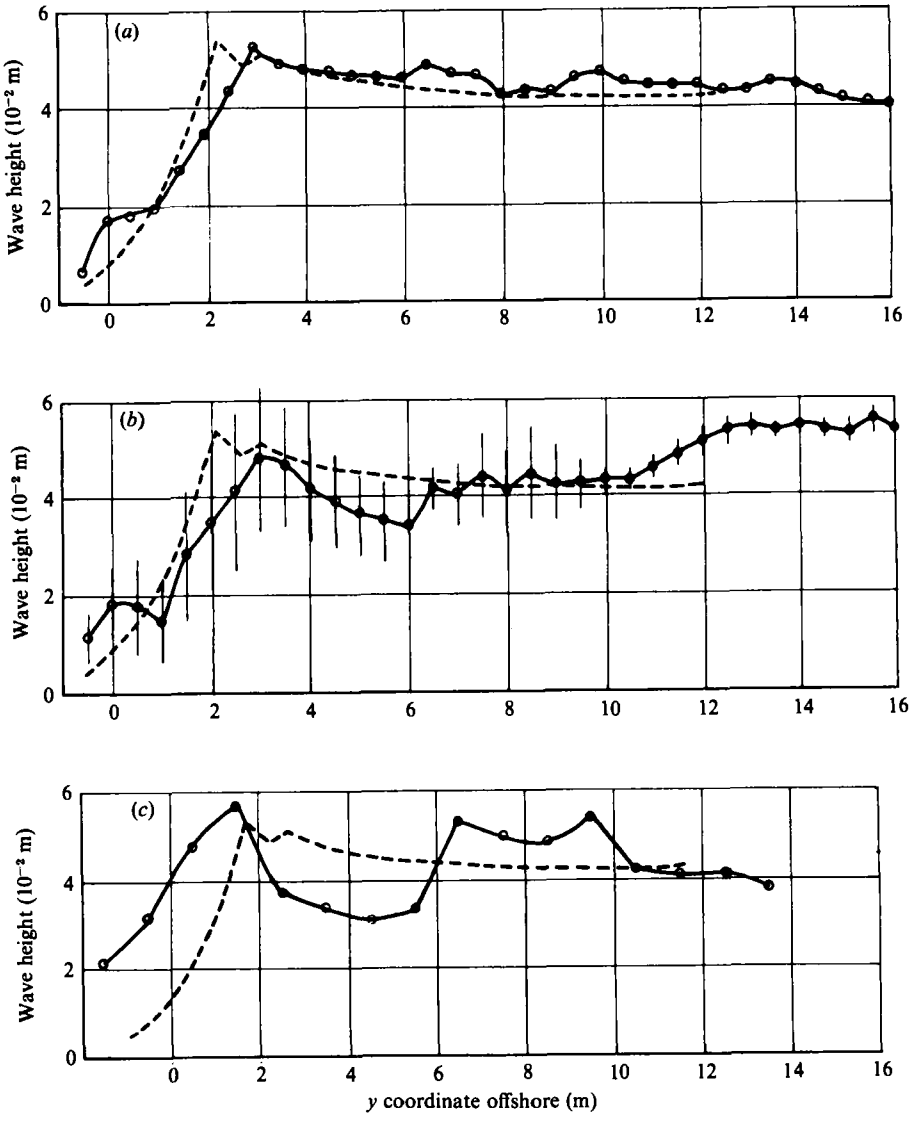

FIGURE 4. Wave-height distributions (——) measured respectively at (*a*) 1.75 m, (*b*) 1.25 m and (*c*) 0.25 m parallel to the downstream sidewall. ----, mean value section IV and V.

wave-height distribution in the rip current region is shown in figures 4 (*b*, *c*). The bars in figure 4 (*b*) show the standard deviation in wave height indicating a large variation in mean wave height in the rip current as a function of time. The average wave set-up measured at the shoreline was 0.005 m, increasing up to 0.01 m near the downstream sidewall.

2.3. *Flow field*

The general features of the current pattern are shown in figure 3. Three zones can be distinguished: the longshore current, the rip current and an eddy. The rip-current velocities have been measured parallel to the *y*-axis in Sections I–III, respectively located at 9.37, 13.37 and 17.37 m from the still-water line (figure 3). The measurements were carried out with a current cross connected to a float and with a specially

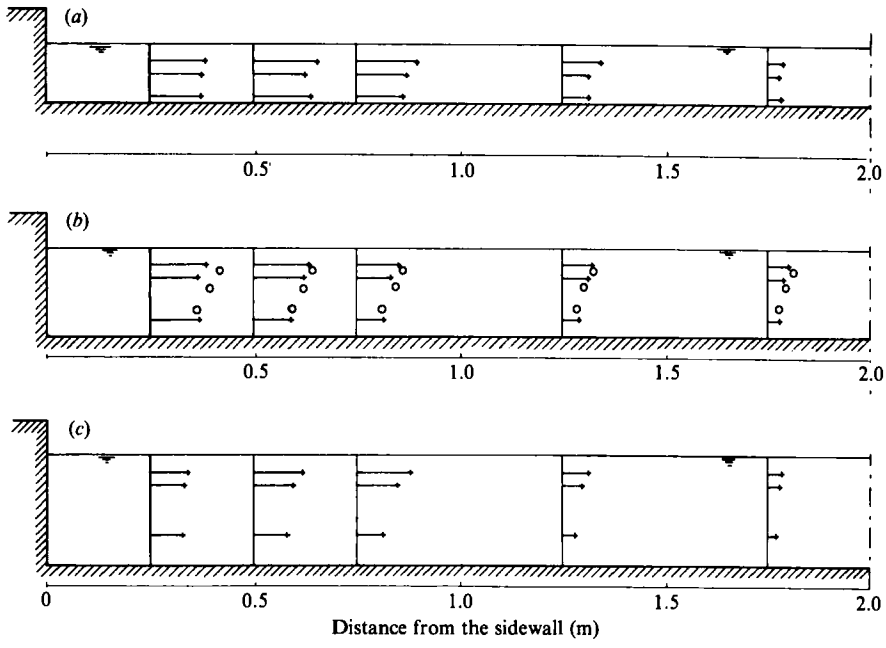

FIGURE 5. Rip-current velocity distribution parallel to the downstream sidewall, measured in (*a*) section I, (*b*) section II and (*c*) section III. +, current cross; ○, micropropeller.

prepared micropropellor. The vertical distribution of the rip-current velocity parallel to the sidewall is shown in figure 5. The circles in figure 5 refer to micropropellor measurements. The measurements carried out with floats are denoted with crosses. The depth-averaged velocities in the rip current are shown as asterisks in figure 9. The longshore-current velocities were measured five times using wet paper cuttings. The average velocities in Sections IV and V are shown as asterisks in figure 7.

Only a limited number of sections have been measured in the experiments since the objective of the test was not to obtain a complete set of data of the velocity field in the basin, but to obtain information about measuring techniques. The data recorded are sufficient to discern interesting details about this current. The longshore-current data are, however, far from complete, but can be used to check the numerical results and to test hypotheses raised during the investigation.

3. Governing equations

3.1. *The flow field*

From figure 5 it can be seen that the vertical velocity profile in the rip current is quite uniform. During the experiments there were no signs of a strongly three-dimensional flow in the basin and, therefore, the flow field u_i has been modelled with the depth-averaged Reynolds equations for unsteady flow assuming a hydrostatic pressure distribution over the vertical, given by

$$\frac{\partial u_i}{\partial t}+u_j\frac{\partial u_i}{\partial x_j}+\frac{1}{\rho}\frac{\partial p}{\partial x_i}+\frac{\tau_{bi}}{\rho h}+\frac{1}{\rho h}\frac{\partial S_{ij}}{\partial x_j}-\frac{1}{\rho h}\frac{\partial}{\partial x_j}(hT_{ij})=0 \quad (i,j=1,2) \tag{3.1}$$

and the continuity equation

$$\frac{\partial}{\partial x_i} u_i h = 0, \tag{3.2}$$

where u_i = velocity component in the i-direction, p = pressure, S_{ij} = radiation stress (integrated over depth), T_{ij} = effective stress, including effects of non-uniform velocity distribution, τ_{bi} = bottom shear stress, h = water depth.

In order to represent the experimental basin in the calculations, the x_1 axis was chosen parallel to the still-water line as shown in figure 3.

The Reynolds equations (3.1) are solved using the ODYSSEE package (Officier, Vreugdenhil & Wind 1986), which was developed at the Delft Hydraulics Laboratory in cooperation with the Laboratoire National d'Hydraulique in France. For the solution the equations are split into functional parts and solved in fractional time steps by means of a finite-difference method. There are no stability limits on the Courant number $\sigma = v\,\Delta t/\Delta x$, where v is the velocity, Δt the time step and Δx the grid spacing. From an accuracy point of view a time step of 10 s has been selected, such that the Courant number does not exceed a value of 3.

As variations in the water level do not play an essential part in the phenomenon, the free surface can be considered as a rigid lid. The pressure head $p/\rho g$ exerted on the lid, will be an approximation of the actual free-surface elevation. Serious errors are introduced only if the variation in mean water level is not negligible relative to the still-water depth, which is the case near the still-water line. We have, therefore, applied a rigid lid in such a way that the mean set-up in the breaker zone is included in the mean water depth and in the wavefield.

An advantage of the ODYSSEE package is that it allows the use of non-orthogonal grids to represent the basin, as shown in figure 6(*d*). The grid spacing has, in fact, been narrowed in the longshore-current and rip-current areas.

3.2. *The wavefield*

As a first approximation the wavefield has been determined by means of a simple refraction formula, excluding wave–current interaction. This has been done because it is expected that outside the breaker zone the driving of the current due to wave–current interaction will be relatively small, as the ratio of maximum current velocity and wave celerity is of the order of 0.1 to 0.2. As the main region of interest is located outside the breaker zone, the wavefield is described by the well-known refraction formula for parallel depth contours:

$$\frac{H}{H_b} = \left[\frac{(c_g)_b \cos\theta_b}{c_g \cos\theta}\right]^{\frac{1}{2}}, \tag{3.3}$$

where the index b refers to the value at the breaker line. The angle θ, between the positive $y(= x_2)$ axis and the direction of wave propagation, has been derived from Snells' law:

$$\frac{\sin\theta}{c} = \text{const.} \tag{3.4}$$

The ratio of group velocity c_g and the wave celerity c, is defined as n, where

$$n = \frac{1}{2} + \frac{kh}{\sinh 2kh}. \tag{3.5}$$

The wave celerity follows from

$$c^2 = \frac{g}{k}\tanh kh, \tag{3.6}$$

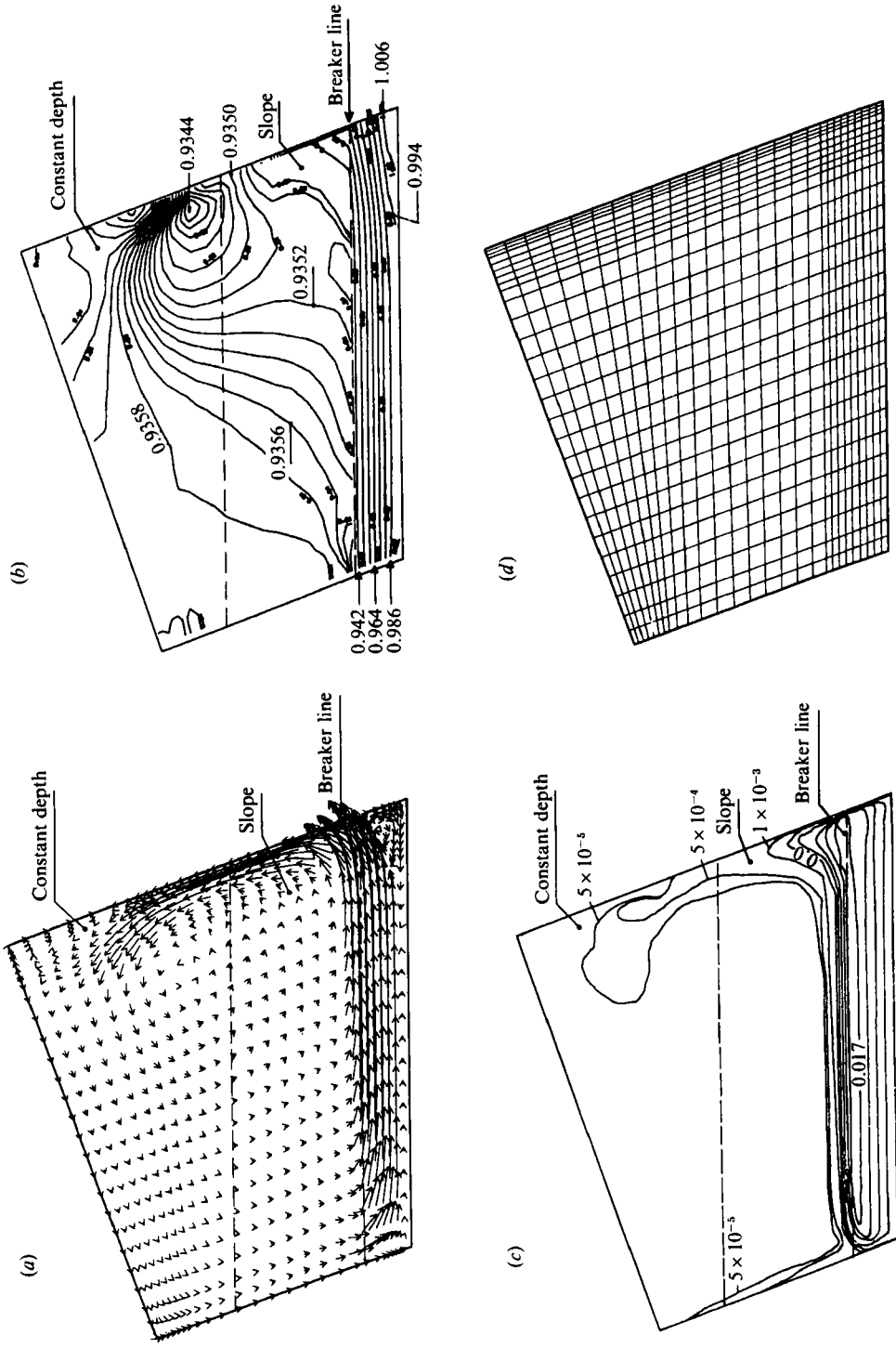

FIGURE 6. Results of the computations using the k–ϵ viscosity model: (*a*) velocity field, (*b*) pressure field p/ρ, (*c*) viscosity field, (*d*) computational grid.

where k is the local wavenumber and h the local water depth. Inside the breaker zone it has been assumed that the wave height H is a constant fraction γ of the mean water depth h or

$$\gamma = H/h. \tag{3.7}$$

The value of γ has been fixed at 0.8, observed at the breaker line. The radiation stress S_{ij} due to wave fluctuations can be written (Longuet-Higgins & Stewart 1964) as

$$S_{xx} = E\{(2n-\tfrac{1}{2})\sin^2\theta + (n-\tfrac{1}{2})\cos^2\theta\}, \tag{3.8}$$

$$S_{xy} = En\cos\theta\sin\theta, \tag{3.9}$$

$$S_{yy} = E\{(2n-\tfrac{1}{2})\cos^2\theta + (n-\tfrac{1}{2})\sin^2\theta\}. \tag{3.10}$$

The wave energy density E for linear progressive waves is equal to $\frac{1}{8}\rho g H^2$.

3.3. *Bottom friction*

The bottom shear stress $\bar{\tau}_b$ is modelled using the weak-flow approximation (Liu & Dalrymple 1978)

$$\bar{\tau}_{bx} = \frac{2}{\pi}\rho C_f \bar{u} u_{max}, \tag{3.11}$$

$$\bar{\tau}_{by} = \frac{4}{\pi}\rho C_f \bar{v} u_{max}, \tag{3.12}$$

where u_{max} is the maximum orbital velocity, which can be expressed for shallow water waves as

$$u_{max} = \frac{1}{2}\frac{H}{h}(gh)^{\frac{1}{2}}. \tag{3.13}$$

Essential in this approach is that the longshore-current velocity is much weaker than and almost normal to the sinusoidal orbital motion (Liu & Dalrymple, 1978). Ryrie (1983*a*), in her study on longshore currents driven by bores, shows that the resulting theoretical bottom friction in the longshore direction is effectively higher for bore motion than for sinusoidal orbital motion.

For the choice of the bottom-friction coefficient we have followed the approach of James (1974). His first conclusion is that for long waves over much of the surf zone, the bottom-friction coefficient is slightly greater than that given by the experiments for steady flow, but of the same order. His second conclusion is that for smooth concrete, as has been used in the laboratory, the flow regime could be transitional or smooth. The friction coefficient found by James ranges for those conditions from 0.002 to 0.003. This is close to the value of 0.0015 that we have used in our computations. Visser (1984) in his thorough analysis of longshore-current data arrives at a similar value. He relates his friction coefficient to the Chezy formula. This procedure allows a simple extrapolation of laboratory results to prototype data, although without removing the necessity of verification.

3.4. *Turbulence*

The lateral stresses T_{ij} can be formulated by means of an eddy viscosity ν_t (Rodi 1980)

$$\frac{1}{\rho}T_{xx} = 2\nu_t\frac{\partial u}{\partial x} - \tfrac{2}{3}k, \tag{3.14}$$

$$\frac{1}{\rho}T_{yy} = 2\nu_t\frac{\partial v}{\partial y} - \tfrac{2}{3}k, \tag{3.15}$$

$$\frac{1}{\rho}T_{xy} = \nu_t\left(\frac{\partial u}{\partial y} + \frac{\partial v}{\partial x}\right). \tag{3.16}$$

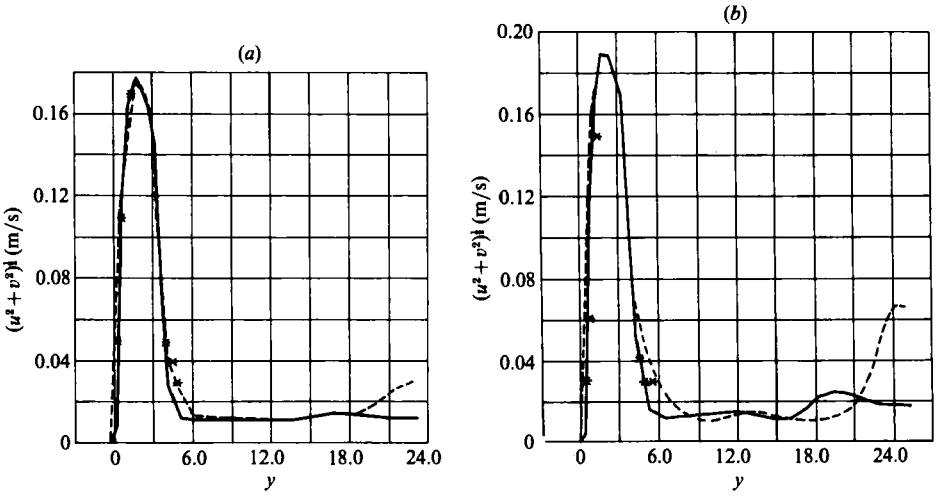

FIGURE 7. Comparison between measured and computed longshore-current velocity profiles in (*a*) section IV and (*b*) section V. ----, constant viscosity; ——, k–ϵ; *, measured values.

A first approximation is to add the turbulent kinetic energy k to the pressure p and estimate the value of ν_t. However, it will be shown in the course of this study that the solution is determined not only by the magnitude of ν_t, but also by its distribution. Three different zones of turbulence intensity can be distinguished in the basin: the rip current, the longshore current and the eddy. Although it is possible to estimate the viscosity distribution in these zones, including the transition areas, we decided to use a k–ϵ model (Rastogi & Rodi 1978; Rodi 1980) which arrives at a more general predictive method by including the effects of generation and dissipation of turbulence due to wave breaking. In the derivation of the effects extensive use has been made of the work of Battjes (1975). The resulting model can be summarized as follows:

$$u\frac{\partial k}{\partial x}+v\frac{\partial k}{\partial y}=\frac{\partial}{\partial x}\left(\frac{\nu_t}{\sigma_k}\frac{\partial k}{\partial x}\right)+\frac{\partial}{\partial y}\left(\frac{\nu_t}{\sigma_k}\frac{\partial k}{\partial y}\right)+P_h+P_{kv}+P_{kw}-\epsilon, \tag{3.17}$$

$$u\frac{\partial \epsilon}{\partial x}+v\frac{\partial \epsilon}{\partial y}=\frac{\partial}{\partial x}\left(\frac{\nu_t}{\sigma_\epsilon}\frac{\partial \epsilon}{\partial x}\right)+\frac{\partial}{\partial y}\left(\frac{\nu_t}{\sigma_\epsilon}\frac{\partial \epsilon}{\partial y}\right)+c_{1\epsilon}\frac{\epsilon}{k}P_h+P_{\epsilon v}+P_{\epsilon w}-c_{2\epsilon}\frac{\epsilon^2}{k}, \tag{3.18}$$

where the P_h, P_{kv} and P_{kw} terms in the k-equation (3.17) refer to the source terms due to velocity shear, bottom friction and the breaking of waves. Similar terms can be found in the ϵ-equation (3.18). The notation of the k–ϵ equations is standard except for P_{kw} and $P_{\epsilon w}$, see Rastogi & Rodi (1978) and Rodi (1980). For the derivation of P_{kw} and $P_{\epsilon w}$ it has been assumed that the turbulent kinetic energy k can be modelled as a function of the energy dissipation rate D/ρ of the breaking waves (Battjes 1975)

$$k=\left(\frac{D}{\rho}\right)^{\frac{2}{3}}. \tag{3.19}$$

The formulation of P_{kw} and $P_{\epsilon w}$ follows from (3.17), (3.18), (3.19), (3.23) and (3.24) if all the source terms except P_{kw} and $P_{\epsilon w}$ are neglected (local equilibrium in uniform flow), leading to

$$P_{kw}=\frac{c_\mu}{M}\left(\frac{D}{\rho}\right)\frac{1}{h};\quad P_{\epsilon w}=c_{2\epsilon}\left(\frac{c_\mu}{M}\right)^2\left(\frac{D}{\rho}\right)^{\frac{4}{3}}\frac{1}{h^2}, \tag{3.20}$$

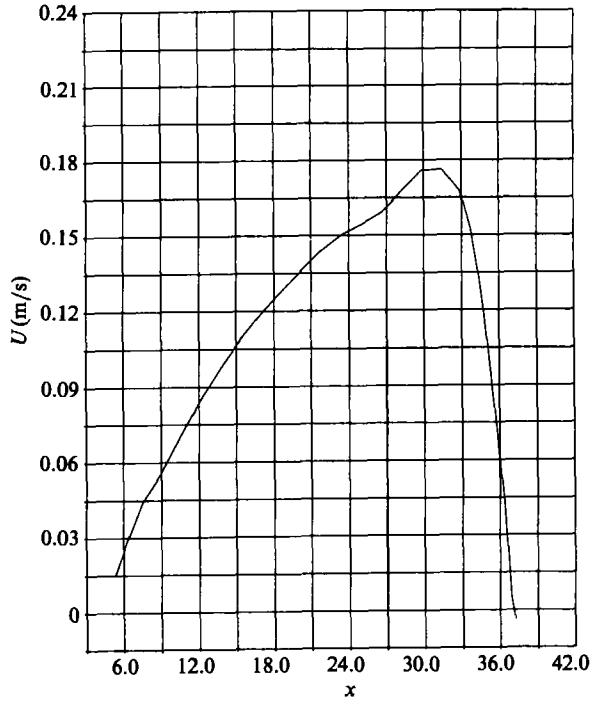

FIGURE 8. Computed longshore current distribution at the breaker line and parallel to the shoreline.

where the dissipation D follows from the energy balance. In the absence of a mean flow the energy balance reduces to

$$\frac{\partial G_x}{\partial x}+\frac{\partial G_y}{\partial y}+D=0, \tag{3.21}$$

in which G_x is the x-component of the time-mean energy flux per unit length. Using a linear wave approximation for $P=Ec_g$ the following dissipation rate results (Battjes 1975):

$$D=-\tfrac{1}{16}\rho g^{\frac{3}{2}}\gamma^2 h^{\frac{5}{2}}\frac{\partial h}{\partial y}\left\{5\cos\theta-\frac{\sin^2\theta}{\cos\theta}\right\}. \tag{3.22}$$

The factor M in (3.20) is of order 1. From experimental data (Visser 1984) a value of 3 has been found, which has been used in the computations. The eddy viscosity ν_t is defined as

$$\nu_t=c_\mu\frac{k^2}{\epsilon}. \tag{3.23}$$

For the case of turbulence produced by breaking waves only, this reduces to the expression given by Battjes (1975):

$$\nu_t=Mh\left(\frac{D}{\rho}\right)^{\frac{1}{3}}. \tag{3.24}$$

However, (3.23) can be used to include the additional effect of velocity shear and bottom friction given by (3.17) and (3.18).

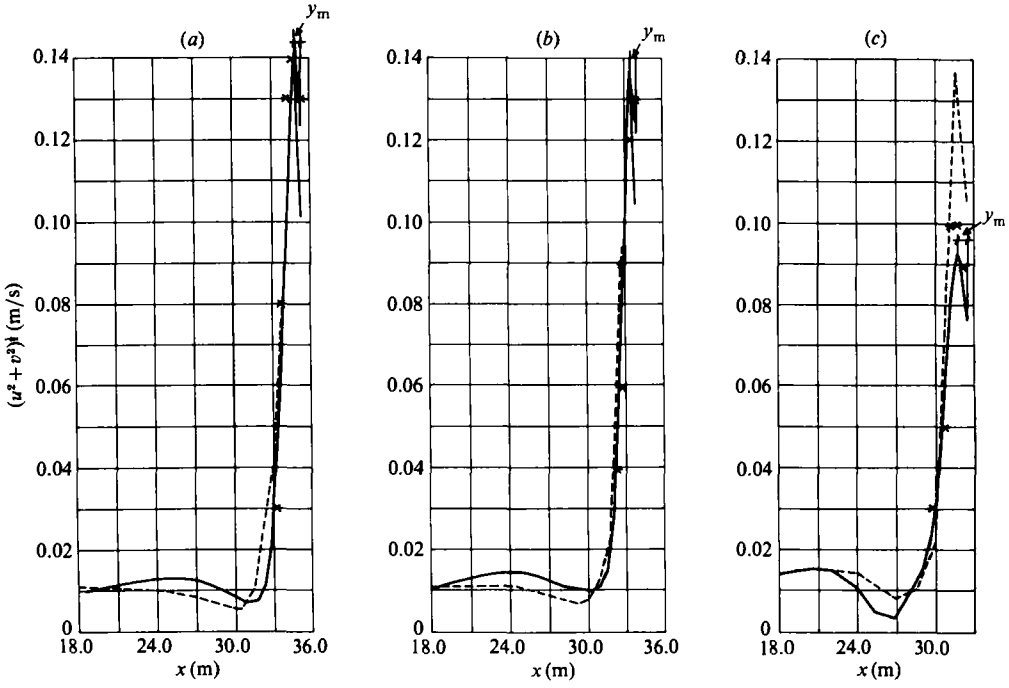

FIGURE 9. Comparison between measured and computed rip-current velocity profiles in (*a*) section I, (*b*) section II and (*c*) section III ----, constant viscosity; ——, k–ϵ; *, measured values.

3.5. *Boundary conditions*

A no-slip condition has been applied along the shoreline, i.e.

$$u = 0. \tag{3.25}$$

The boundary condition along the wavemaker has been assumed to be a free slip velocity u_t, where

$$\frac{\partial u_t}{\partial n} = 0. \tag{3.26}$$

The law of the wall has been applied along the sidewalls. It is considered that this set of boundary conditions agrees reasonably with the conditions observed in the basin.

4. Numerical results

The results of the numerical computations are shown in figures 6–11. A direct comparison with the laboratory measurements is given in figures 7 and 9. A good agreement is observed. It should be noted that a considerable longshore current exists outside the breaker zone. This circulating current is partially explained by the fact that the basin is closed.

A comparison in figure 7 of the observed velocity profiles with the longshore-current theory of Longuet-Higgins (1970) with $N = 0.01$ shows that the theoretical maximum velocity is of the order of 0.35 m/s. This theoretical velocity is higher than the observed maximum velocity, because the longshore current in the basin is by no means uniform. This point is made clear in figure 8 where the longshore variation

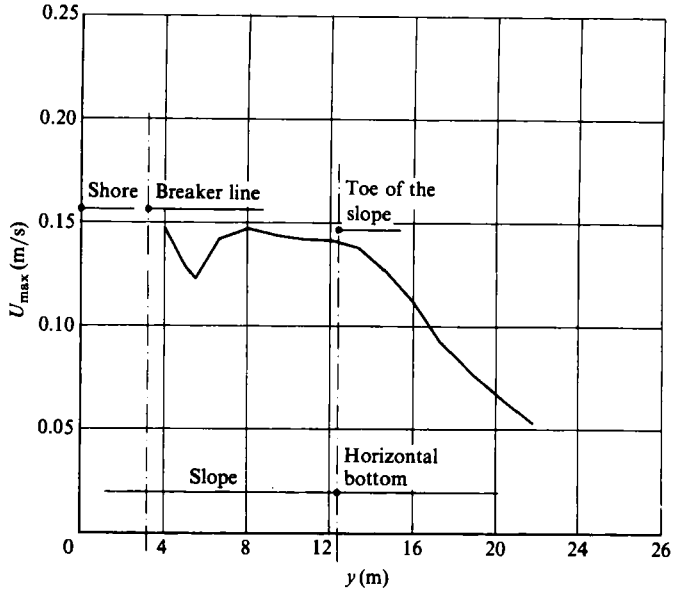

FIGURE 10. Computed maximum rip current velocity.

of the longshore velocity at the breaker line is shown. Outside the breaker zone the observed velocity becomes higher than the theoretical velocity. This is due to the large eddy that is present in the basin. The conclusion is that the conditions in the present tests do not meet the prerequisites of the theory of Longuet-Higgins for uniform longshore currents. The magnitude of the rip current (figures 9 and 10) remains practically constant on the sloping part of the bottom. In the constant-depth region, the rip current spreads rapidly and separates from the wall, which is reflected in the pressure distribution (figure 6*b*). It is not known whether this happened in the experiment. Also it is not quite certain whether the numerical results are in completely steady state in the separation region. However, the rapid decrease of rip-current velocity is clearly seen in the measurements and the computational results of Section III (figure 9).

5. The importance of convection

Figures 10 and 11 (*a*) show that the rip current on the sloping bottom behaves like a jet with constant maximum velocity and decreasing width. This convergence of streamlines was explained by Arthur (1962) from the vortex-stretching effect. As this is described by the convective terms in the momentum equations, it can be concluded that the rip current is convection-dominated in the region. The same conclusion can be drawn from an estimate of the order of magnitude of the various terms in the momentum equations. To support this conclusion, a numerical experiment was done with a constant depth offshore from the depth contour of 0.09 m, but with all the other parameters unchanged. The vortex-stretching effect should not occur in this case. The result is shown in figure 11 (*b*) and it is seen that the convergence of streamlines has disappeared.

Another numerical experiment to illustrate the importance of the convective terms is to switch them off altogether. The result of this is shown in figure 11 (*c*). The rip

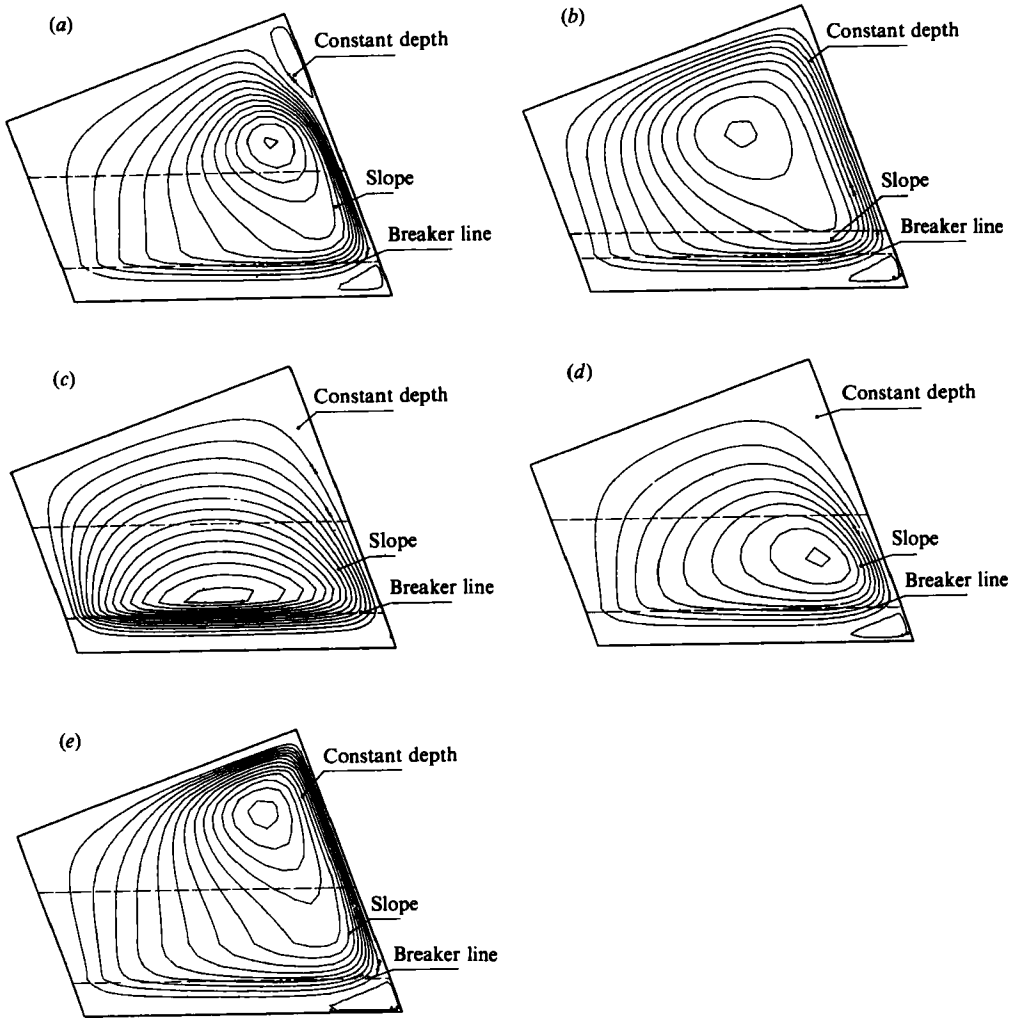

FIGURE 11. Computed streamlines for various conditions of the basin shown in figure 6. $\Delta\psi = 0.004$ m^2/s. (*a*) Condition shown in figure 7; (*b*) depth remains constant offshore of the 0.09 m depth contour; (*c*) convective terms are switched off; (*d*) constant viscosity outside the breaker zone $\nu_t = 0.03$ m^2/s; (*e*) constant viscosity outside the breaker zone $\nu_t = 10^{-5}$ m^2/s.

current has now disappeared completely, as expected. It is observed that almost all closed streamlines pass through the breaker zone, where the driving forces for the flow are located. This follows from the vorticity balance in the absence of viscosity, as discussed in §6.

6. The importance of viscosity

For a good understanding of the importance of the magnitude of viscosity, the vorticity balance is a useful tool. For a depth-averaged flow, this has been used by Flokstra (1977). Extending his analysis with driving forces, it is found that

$$\frac{\partial \omega}{\partial t}+\frac{\partial}{\partial x}u\omega+\frac{\partial}{\partial y}v\omega+\frac{\partial}{\partial y}\frac{\tau_{bx}}{\rho h}-\frac{\partial}{\partial x}\frac{\tau_{by}}{\rho h}+\frac{\partial}{\partial y}\frac{F_x}{\rho h}-\frac{\partial}{\partial x}\frac{F_y}{\rho h}-\nu\left(\frac{\partial^2\omega}{\partial x^2}+\frac{\partial^2\omega}{\partial y^2}\right)=0, \qquad (6.1)$$

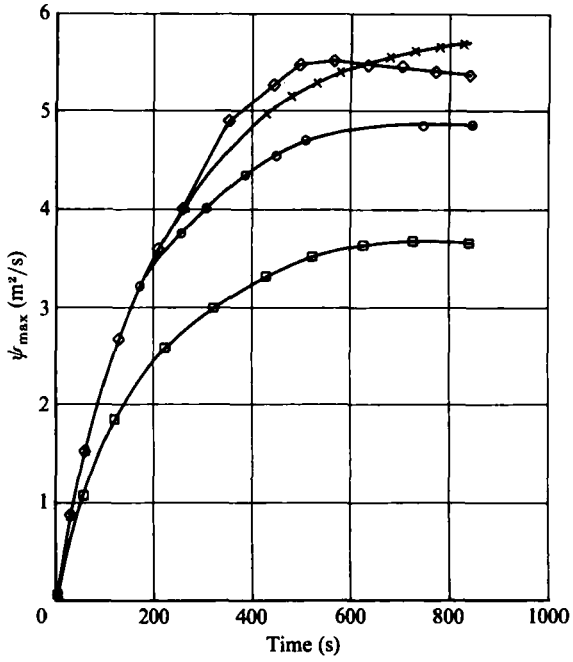

FIGURE 12. Circulating discharge as a function of time for the k–ϵ viscosity model (○), constant-viscosity model (◇, low viscosity; □ high) and without the effect of the convective terms (×, convective terms switched off).

where
$$F_x = \frac{\partial S_{xx}}{\partial x} + \frac{\partial S_{xy}}{\partial y}; \quad F_y = \frac{\partial S_{yx}}{\partial x} + \frac{\partial S_{yy}}{\partial y} \tag{6.2}$$

and
$$\omega = \frac{\partial v}{\partial y} - \frac{\partial u}{\partial x}. \tag{6.3}$$

For simplicity, the viscosity ν has been taken as constant here. For steady-state flow, integration over an area enclosed by streamline S gives

$$\int_S \frac{1}{\rho h} \left\{ \tau_{bs} + F_s - \mu h \frac{\partial \omega}{\partial n} \right\} ds = 0, \tag{6.4}$$

where $\mu = \rho\nu$ is the dynamic viscosity. If there are no driving forces or shear stresses along the contour S, it is seen that the circulation of the bottom shear stress should vanish. As the bottom stress is proportional to the flow velocity, it is concluded that there cannot be any circulation, i.e. such a closed streamline cannot exist. Therefore, for flows with a small influence of viscosity, but dominated by bottom friction, all closed streamlines (if any) should pass through the breaker zone where $F_s \neq 0$. This is almost the case of figure 11(*c*) where bottom friction is strongly dominant over (lateral) viscosity.

A different situation is obtained, only if viscosity is increased to a physically unrealistic level. This is shown in figure 11(*d*), where the viscosity outside the breaker zone is kept at the (high) level of about 3×10^{-2} m²/s obtained from Longuet-Higgins' theory at the breaker line. Convection is no longer dominant in this case and consequently the rip current disintegrates rapidly. Closed streamlines can be supported outside the breaker region by the lateral shear stress.

If the viscosity outside the breaker zone is kept constant at the low level of 10^{-5} m^2/s (with a smooth transition just outside the breaker line) another numerical experiment shows that the main features of the flow are still represented (figure 11*e*). This leads to the conclusion that the magnitude of the viscosity is not very important, provided that it is not unrealistically large.

However, there are differences of detail between figures 11(*e*) (with constant viscosity), and 11(*a*) (with viscosity distribution as given in figure 6*c*, obtained from the k–ϵ model). Also, figure 9 shows that the decrease of rip-current velocity in the constant-depth region is no longer reproduced. Apparently, according to the measurements, for such details the distribution of viscosity is important.

7. Importance of bottom friction

In figure 12 the total flow rate between the centre of the eddy and the sidewall of the basin is given as a function of time for the various numerical experiments. It is seen that the flow rate attains roughly the same value for all realistic viscosity distributions: only the one with an extremely high viscosity gives a different flow rate. This means that the viscosity (provided it is in a realistic range) does not determine the flow rate in the rip current. Moreover, it is seen that switching off the convective terms does not significantly change the flow rate, so this is not the determining factor either. It must therefore be concluded that the bottom friction is the only mechanism that regulates the flow rate in the rip current, as it is the remaining term in the momentum equations. This has not been verified by a separate numerical experiment.

8. Length- and timescales for coastal currents

In figure 8 it can be seen that the longshore current is accelerating almost over the full length of the basin. This indicates a lengthscale that is relevant for the distance between groynes along a sandy beach. Similarly figure 12 indicates a timespan that is required for the nearshore current system to develop. These length- and timescales can also be derived from the vorticity equation (6.1) in streamwise coordinates s, n:

$$\frac{1}{Uh}\frac{\partial \omega}{\partial t}+\frac{\partial}{\partial s}\left(\frac{\omega}{h}\right)+\frac{C_f H g^{\frac{1}{2}}}{\pi U h^{\frac{3}{2}}}\left\{\frac{\omega}{h}+\frac{3}{2}\frac{U}{h}\frac{\partial h}{\partial n}\right\}+\frac{1}{Uh}\frac{\partial}{\partial s}\frac{F_s}{\rho h}-\frac{\nu}{q}\Delta_{s,n}\omega=0, \tag{8.1}$$

where $\Delta_{s,n}$ represents the Laplace operator in streamwise coordinates. An estimate of the timescale over which a disturbance in the longshore-current velocity reduces to a factor of e^{-1} of the original value follows from a balance between the time derivative and the bottom friction, i.e.

$$T=\frac{\pi h^{\frac{3}{2}}}{C_f H g^{\frac{1}{2}}}. \tag{8.2}$$

This timescale is similar to that derived by Ryrie (1983*b*), who considered the timescale in the generation of longshore currents driven by breaking of bores. The difference between the timescale found in (8.2) and that found by Ryrie results from a different formulation of bottom friction.

In the experiments the conditions in the rip current were $H = 0.043$ m, $C_f = 0.0015$ and an average water depth of about 0.15 m. The timescale resulting from (8.2) was 900 s. This value is in agreement with the timescale shown in figure 12.

For prototype conditions, $H = 1$ m, $C_f = 0.01$ and a mean water depth of 3 m, the timescale is 520 s. Clearly the basin is rather smooth compared with prototype conditions. However, it can be concluded for both conditions that it takes a considerable time for a rip current to develop.

A first estimate of the lengthscale for the generation of the nearshore current system follows from (8.2) multiplied by an average velocity U:

$$L = \frac{\pi U h^{\frac{3}{2}}}{C_f H g^{\frac{1}{2}}}. \tag{8.3}$$

For the test conditions in the longshore current of $U = 0.20$ m/s, $h = 0.04$ m, $C_f = 0.0015$ and $H = 0.03$ m, a value of $L = 36$ m results. This value is in reasonable agreement with the lengthscale that can be inferred from figure 8. In a rip current the momentum is dissipated by bottom friction and viscosity. The lengthscale of the rip current related to bottom friction is similar to (8.3).

The length- and timescales presented in this section are only indicative as viscosity and variations in bottom topography ($\partial h/\partial n$) and geometry of the basin should be taken into account for a more precise estimate.

9. Conclusions

The wave-induced circulation system in a closed basin can be subdivided into the longshore current, the rip current and an eddy (figure 3).

The rip current is strongly dominated by convection. If convective terms are excluded, the rip current disappears (figure 11*c*). The combined effect of the bottom topography and convective terms causes the streamlines of the rip current on a seaward-sloping bottom to converge (Arthur 1962). If the bottom remains horizontal the rip current is still present, but the streamlines remain straight (figure 11*b*). An additional effect of the sloping bottom is that the maximum velocity in the rip current remains more or less constant. The effect of bottom friction is to decelerate the rip current and to induce a divergence of the streamlines. The timescale for the generation of rip currents is given by (8.3) and for prototype conditions this is of the order of 10 min.

The circulation system shown in figure 11(*a*) is enforced by the closed basin. Whether or not such circulation systems will occur along a sandy beach protected by a series of groynes depends on geometrical parameters, such as the length of the groynes and distances between them, and also on physical parameters such as bottom roughness and wave characteristics. The current system has also been interpreted in terms of the vorticity balance. It is concluded that vorticity resulting from oblique breaking of waves is largely dissipated by bottom friction and to a minor extent by viscous shear. The bottom-friction coefficient C_f determines in that case the discharge $\psi_{\max}$ through a line connecting the centre of the eddy with the sidewall. Although the viscous terms in the eddy appear to be much smaller than the bottom friction, precisely these terms are allowing for closed streamlines situated outside the breaker zone (figure 11*a*).

Finally, it has been concluded that for a detailed reproduction of the velocity field of the rip head adjacent to the structure, a turbulent viscosity field as obtained from a higher-order turbulence model such as a k–ϵ model, is essential.

These conclusions are particularly important for extrapolation to prototype conditions. In the papers mentioned in §1, the viscosity coefficients used outside the breaker zone are in general several orders of magnitude too large. If the flow field

around groynes and harbour moles is computed based upon those suggestions, the rip currents will disintegrate much too fast.

The authors wish to acknowledge the programming effort of Mr C. ten Napel at the initial stage of the project and the contribution of Mr Jin Zhongqing during the execution of the study. The use of the figure 1 by Dr P. Cowell, of a rip-current formation north of Sydney (Australia) is gratefully acknowledged.

REFERENCES

ARTHUR, R. S. 1962 A note on the dynamics of rip currents. *J. Geophys. Res.* **67**, 2777–2779.

BATTJES, J. A. 1975 Modelling of turbulence in the surf zone. In *Symp. on Modelling Techniques, San Francisco*, Vol. 2, pp. 1050–1062, ASCE.

BOWEN, A. J. 1969 Rip currents I, theoretical investigations. *J. Geophys. Res.* **74**, 5467–5478.

DALRYMPLE, R. A., EUBANKS, R. A. & BIRKEMEYER, W. A. 1977 Wave induced circulation in shallow basins. *Trans. ASCE* **WW1**, 117–135.

EBERSOLE, B. A. & DALRYMPLE, R. A. 1979 A numerical model for nearshore circulation including convective accelerations and lateral mixing. *Ocean Engineering rep.* 21, University of Delaware, Delaware.

FLOKSTRA, C. 1977 The closure problem for depth averaged two-dimensional flow. *Publ.* 150. Delft Hydraulics Laboratory.

JAMES, I. D. 1974 A non-linear theory of Longshore Currents. *Estuar. Coast. Mar. Sci.* **2**, 235–249.

KAWAHARA, M. & KASHIYAMA, K. 1984 Selective lumping finite element method for nearshore current. *Intl J. Numer. Methods in Fluids* **4**, 71–97.

KAWAHARA, M., TAKAGI, T. & INAGAKI, K. 1980 A finite element method for nearshore current. In *3rd Intl Conf. on Finite Element Methods in Flow Problems, Banff*, pp. 70–79.

LIU, P. L. F. & DALRYMPLE, R. A. 1978 Bottom frictional stresses and longshore currents due to waves with large angles of incidence. *J. Mar. Res.* **36**, 357–375.

LIU, P. L. F. & MEI, C. C. 1976 Water motion on a beach in the presence of a breakwater. *J. Geophys. Res.* **81**, 3079–3094.

LONGUET-HIGGINS, M. S. 1970 Longshore current generated by obliquely incident sea waves, 1, 2. *J. Geophys. Res.* **75**, 6778–6801.

LONGUET-HIGGINS, M. S. & STEWART, R. W. 1964 Radiation stress in water waves, a physical discussion with applications. *Deep-Sea Res.* **11**, 529–562.

OFFICIER, M. J., VREUGDENHIL, C. B. & WIND, H. G. 1986 Applications in hydraulics of a curvilinear finite difference method for the Navier–Stokes equations. In *Recent Advances in Numerical Fluid Dynamics* (ed. C. Taylor). Pineridge.

RASTOGI, A. K. & RODI, W. 1978 Predictions of heat and mass transfer in open channels. *J. Hydraul. Div. ASCE* No. Hy 3, 397–420.

RODI, W. 1980 Turbulence models and their application in hydraulics. Institut für Hydromechanik and Sonderforschungsbereich 80, University of Karlsruhe, Karlsruhe, Germany, 104.

RYRIE, S. C. 1983*a* Longshore motion generated by obliquely incident bores. *J. Fluid Mech.* **129**, 193–212.

RYRIE, S. C. 1983*b* Longshore motion due to an obliquely incident wave group. *J. Fluid Mech.* **137**, 273–284.

STIVE, M. J. F. & WIND, H. G. 1982 A study of radiation stress and set-up in the nearshore region. *Coastal Engng* **6**, 1–25.

TAM, C. K. W. 1973 Dynamics of rip currents. *J. Geophys. Res.* **78**, 1937–1943.

VISSER, P. J. 1984 Uniform longshore current measurements and calculations. In *Proc. of the 19th Coastal Engng Conf, Houston*, vol. 2, pp. 2192–2208. ASCE.

WATANABE, A. 1982 Numerical models of nearshore currents and beach deformation. *Coastal Engng Japan* **25**, 147–161.

WU, C. S. & LIU, P. L. F. 1982 Finite element modelling of breaking wave induced nearshore current. In *Finite Element Flow Analysis* (ed. T. Kawai), pp. 579–586. North Holland.